The crystallinity and piezoelectric properties of spray-coated films of P(VDF70-TrFE30): effect of film thickness and spin-crossover nanofillers

Jose Elias Angulo Cervera, Mario Piedrahita-Bello, Baptiste Martin, Eric Dantras, Liviu Nicu, Thierry Leichlé, Kevin Dalla Francesca, Antonio da Costa, Anthony Ferri, Rachel Desfeux, et al.

ARTICLE

Crystallinity and piezoelectric properties of spray-coated films of P(VDF_{70}-$TrFE_{30}$): effect of film thickness and spin-crossover nanofillers

Received 00th January 20xx,
Accepted 00th January 20xx

DOI: 10.1039/x0xx00000x

José Elías Angulo-Cervera,[a,b] Mario Piedrahita-Bello, [a,b] Baptiste Martin,[a,c] Eric Dantras,[c] Liviu Nicu,[b] Thierry Leichle,[b,d] Kevin Dalla Francesca,[e] Antonio Da Costa,[e] Anthony Ferri,[e] Rachel Desfeux,[e] Lionel Salmon,[a] Gábor Molnár[a,*] and Azzedine Bousseksou[a,*]

Spray coating the ferroelectric polymer P(VDF-TrFE) appears as an attractive approach for the fabrication of electromechanical transducers. However, it is important to elucidate how the crystallinity and associated piezoelectric properties depend on the coating thickness and additives. To this aim, we have spray-coated various substrates both with pure and nanocomposite films of the 70-30 % copolymer in a broad thickness range (200 nm – 30 µm). Using X-ray diffraction, differential scanning calorimetry, Raman spectroscopy and atomic force microscopy, we show that the obtained films are dense and homogeneous with ca. 50 % crystallinity, which consists of a majority polar phase, with slight alterations in the sub-micrometer thickness regime. Robust piezoelectricity and ferroelectricity are revealed at room temperature through both local hysteresis loops and lithography experiments using the piezoresponse force microscopy technique. After poling, the piezoelectric d_{33} coefficient displays values up to -19 and -11 pC/N for the pure copolymer and the composite, respectively. For a 33 vol% load of inorganic spin-crossover nanofiller, the switching properties are substantially improved and a coercive voltage <10 V is demonstrated for micrometric films. Overall, this approach appears as a promising way for the in-situ integration of high quality piezopolymer films into complex transducer geometries for sensing, actuating and energy harvesting purposes.

Introduction

Poly(vinylidene fluoride), PVDF and its copolymers have been widely investigated for their appealing piezo-, pyro- and ferroelectric properties. Their ability to convert mechanical strain to electrical charge, and vice versa, have been already exploited in various applications, such as energy harvesting, sensing, monitoring and mechanical actuation [1-3]. Besides the attractive electromechanical properties, this family of piezopolymers possesses also high mechanical flexibility, low weight and good manufacturability. In particular, their good solubility and low melting point allows to manufacture them using various solution- and melt-based techniques, such as spin coating, electrospinning, Langmuir-Blodgett method, blade casting, hot pressing, screen-printing, inkjet printing roll-to-roll processing and 3D-printing [4-6] and integrate them into micromechanical devices [7-8]. In each case, a careful optimization of deposition conditions (speed, solvent, temperature, …) is mandatory and post-deposition treatments (annealing, poling) are usually indispensable to obtain films with good piezoelectric properties.

Among the numerous crystalline polymorphs of PVDF [9-12], the so-called β-phase is the most attractive structure for electromechanical applications. It has an all-trans, planar zigzag conformation with natural electrical polarity [13]. This is the crystalline form with the highest spontaneous polarization, dielectric constant and piezoelectric coefficient. Although this all-trans phase is not favoured in PVDF, it can be directly obtained from a copolymerization process with the addition of tetrafluoroethylene, TrFE, units (from around 17 mol%). Due to the steric hindrance of the bulkier TrFE groups, P(VDF-TrFE) chains adopt more easily an all-trans (TTTT), low-temperature unit cell, being polar from the beginning and requiring no stretching or drawing to improve its ferroelectric properties [11,14]. This phase is often designated as β-phase owing to its strong similarity to the PVDF β-phase. The fact that the polar phase can be obtained in P(VDF-TrFE) copolymers without mechanical treatments is particularly important for applications requiring film coatings. Indeed, P(VDF-TrFE) has a semi-crystalline structure, with crystallinity typically found between 35-70 %, depending on various parameters during the polymerization, the fabrication process and the TrFE content [4]. Recently, there have been a growing interest in using spray coating as a technologically relevant method for manufacturing P(VDF-TrFE)-based coatings. Spray coating refers to a family of

[a] LCC, CNRS & University of Toulouse, 205 route de Narbonne, Toulouse 31077,France. E-mail: azzedine.bousseksou@lcc-toulouse.frgabor.molnar@lcc-toulouse.fr
[b] LAAS, CNRS & University of Toulouse, 7 avenue du Colonel Roche,Toulouse 31400, France
[c] CIRIMAT, CNRS & University of Toulouse (UPS, INPT), 118 Route de Narbonne, 31062 Toulouse, France
[d] Georgia Tech-CNRS International Research Laboratory, School of Electrical and Computer Engineering, Atlantic Drive, Atlanta, GA, 30332,USA
[e] Univ. Artois, CNRS, Centrale Lille, Univ. Lille, UMR 8181 – UCCS – Unité de Catalyse et Chimie du Solide, F-62300 Lens, France.
Electronic Supplementary Information (ESI) available: Additional sample characterization data. See DOI: 10.1039/x0xx00000x

techniques, which allow to turn a fluid into a mist (using, for example, a compressed gas) and spray it onto the target surface through a nozzle. Spray coating has the advantage of being able to achieve large-area, conformal deposition of various materials on non-flat, complex surfaces [15-16]. Notably, *in situ* coating of structural parts by piezoelectric polymers have been employed recently to fabricate ultrasonic transducers for structural health monitoring [17-19], strain actuators for adaptive optics [20], microelectromechanical systems (MEMS) [21] and piezo/ferroelectric coatings [22-23]. In the present work, we investigate the feasibility of high-quality P(VDF-TrFE) films by means of spray-coating. The piezoelectric behaviour of the films of different thicknesses (from ca. 200 nm to 30 μm) is correlated with their crystallinity, which is the key material property in this context. Besides the investigation of the pure polymer films, we explore also the effect of inorganic, spin crossover (SCO) nanofillers on the piezoelectric properties. Indeed, the possibility of spray-coating electroactive composite films provides a first key step towards the development of useful product properties between the electromechanical behaviour of the polymer and the spontaneous strain in the SCO filler [24-25].

Experimental Section

Coating process

Samples were fabricated with a polymeric matrix of P(VDF-TrFE) with a ratio of vinilydene/trifluoroethylene of 70/30, provided by Piezotech. The inorganic SCO nanofillers with formula $[Fe(Htrz)_{2.05}(trz)_{0.75}(NH_2trz)_{0.2}](BF_4)_{1.25}$ were synthetized using a reverse micelle technique previously described in the literature [26]. The coating fluid was prepared by dissolving 1 g P(VDF-TrFE) in 20 ml 2-butanone at 50 °C, followed by stirring for 30 minutes and then adding acetone to the mixture until a total volume of 150 ml was achieved. For nanocomposite coatings, the fluid was prepared by dispersing the SCO nanofillers (0.5 g) in 15 ml 2-butanone via sonication during 10 minutes. A P(VDF-TrFE) solution (1g in 20ml 2-butanone) was then added to the particle suspension, which was then homogenized by stirring. Finally, acetone was added to the mixture until a total volume of 150 ml was achieved. This mixture of solvents was found beneficial for the final film quality – possibly due to a more appropriate dispersion or viscosity. The sample was then homogenized in an ultrasound bath for 30 minutes. The coating solutions were then sprayed over different types of substrates, including silicon, fused silica, Teflon and gold, using a SUSS MicroTec AltaSpray 8 manual spray coater. The substrates were pre-cleaned by rinsing them successively in acetone, deionized water and ethanol, followed by plasma cleaning in a PVA TePla 300 microwave plasma system with 1 l/min O_2 flow and 800 watts power for 5 minutes. During the coating process, the substrates were held at 65 °C to ensure fast evaporation of the solvent. Spraying was carried out with flow rates between 1.1 and 3.3 ml min^{-1}, a gas pressure of 5 bar, a sample - nozzle distance of 20 cm, a pitch of 4 mm between adjacent scanning lines and a speed of 120 mm/s for the spray arm (see also Fig. S1 in the Supporting Information, SI). The as-deposited films were finally annealed at 105 ºC for 30 min.

Sample characterization

The thickness of the films was assessed using a Tencor P17 profilometer. The surface topography of the samples was characterized by means of a Cypher-ES (Oxford Instruments) atomic force microscope (AFM) in Tapping mode. Scanning electron microscopy (SEM) imaging was conducted by means of a HITACHI S-4800 instrument.

Grazing incidence X-ray diffractograms (GIXRD) of thin films were acquired at room temperature on a PANanalytical X'Pert PRO MPD system in a parallel beam configuration using Cu-K_α radiation. The incident beam optics consisted of a mirror with a 1/32° divergence slit. A parallel plate collimator (0.18°) and Soller slits (0.04°) were mounted on the path of the diffracted beam. An X'Celerator detector in receiving slit mode was used for X-ray collection. The thickest films (30 μm) were analysed using the same instrument in Bragg-Brentano geometry. Variable temperature Raman spectra were acquired using an XploRA micro-spectrometer (Horiba) with a spectral resolution of ca. 5 cm^{-1}. The laser beam (532 nm, 0.1 mW) was focused on the sample by a 50× magnification microscope objective, which was also used to collect the scattered light. The Rayleigh scattering was removed by an edge filter. The sample temperature was controlled by a THMS600 heating-cooling stage (Linkam Scientific). Differential scanning calorimetry (DSC) measurements were carried out using a Thermal Analysis DSC 2920 instrument with a heating ramp of 10 °C/min from 30 to 180 °C. Temperature and enthalpy were calibrated using the melting transition of a high purity indium sample.

Piezoelectric properties

The piezoelectric properties of the samples have been assessed using two different approaches. Thick, freestanding samples were poled between gold-coated stainless steel disks using an Agilent 33220A waveform generator and a Trek high voltage amplifier. Several cycles of a sinusoidal poling electric field up to 60 MV/m were applied at a frequency of 100 mHz at room temperature. During poling, the samples were immerged in silicon oil to prevent arcing. The piezoelectric coefficient d_{33} was measured 24 h after the poling step, using a PM-200 piezometer (Piezotest), with an applied force of 0.25 N at 110 Hz frequency. Thin films, deposited on gold-coated silicon substrates, were locally investigated using piezo-force microscopy (PFM) technique. PFM analyses were carried out by means of an MFP-3D (Asylum Research/Oxford Instruments) microscope in dual AC resonance tracking (DART) mode [27] under ambient conditions using Pt/Ir-coated probes (PPP-EFM, NanoSensors) and stiff cantilevers (k ~ 3.9 N/m). PFM in spectroscopic mode (piezoloops recording) was conducted by grounding the conductive substrate and applying an AC driving voltage of 2 V to the probe. Piezoloops were recorded in remnant mode, i.e., DC voltage pulses are applied to the active layer and the PFM signal is measured at zero field. Poling experiments were performed by applying DC voltages of opposite polarity to the probe while scanning the sample surface.

Results and discussion

Film preparation and morphology

Using the optimized coating parameters (see Experimental), we were able to deposit P(VDF-TrFE) layers with controlled thicknesses between 200 nm and 1 µm in a single spray-cycle. Thicker films, up to 30 µm thickness, were obtained by multilayer deposition. The resulting films are highly transparent and can be fixed on various substrates or exist as freestanding films (Fig. 1). Indeed, films above ca. 5 µm thickness, deposited on antiadhesive substrates (e.g. Teflon), can be peeled off and used as stand-alone samples.

After film deposition, a recrystallization process is necessary in order to enhance the amount of the polar phase in the P(VDF-TrFE) matrix. To this aim, the films were annealed at 105 ºC, i.e. near the Curie temperature. This annealing temperature has been chosen in order to be able to compare the results with our previous report on *ca.* 0.1 mm thick blade casted films of similar composition [25]. One must note, however, that somewhat higher annealing temperatures could provide even better crystallinity [11] (see Fig. S2 for a case study). Nevertheless, a reasonably good crystallinity is reached already at 105 °C (*vide infra*), allowing for a straightforward comparison of the various samples.

Figure 1. Top panel: Representative photographs of a P(VDF-TrFE) coated glass substrate and a 10 µm thick freestanding film. Bottom panel: SEM images of a 800 nm thick P(VDF-TrFE) coating deposited on a microstructure. (A scratch was made to reveal the coating.)

For the fabrication of P(VDF-TrFE) nanocomposites, we used an inorganic, spin crossover (SCO) filler. In brief, SCO compounds are phase change materials, which can give rise to high thermal strain at the phase transition [28]. This strain can be then used for mechanical actuation purposes [29]. In particular SCO@P(VDF-TrFE) composites were used to actuate MEMS [30] or other types of mechanical systems [31], but the strain can be also coupled to the piezoelectric properties of the P(VDF-TrFE) matrix to provide original (thermo-electrical) product properties [24-25]. In the present work, we charged the polymer matrix with 33 vol% nanocrystalline SCO compound with the chemical formula $[Fe(Htrz)_{2.05}(trz)_{0.75}(NH_2trz)_{0.2}](BF_4)_{1.25}$ (trz = 1,2,4-triazolato) [26]. Transmission electron microscopy (TEM) images revealed elongated, prolate-shaped particles with ca. 200 and 20 nm mean length and diameter, respectively (see Fig. S3). It is important to note that the particles were synthesized using a reverse-micelle based method. We found that this type of particles are less prone to aggregation, which is a primary concern in spray coating, implying relatively long transit times between the mixing of the constituents and their deposition on the surface.

SEM images show that the films cover uniformly the whole substrate surface, including edges, which is an advantage for piezoelectric applications as short circuits and discharge are less prompt to occur (Fig. 1, see also Fig. S4). Locally the pure copolymer films appear very smooth and homogeneous, although one can note the formation of a few bubbles on large-scale SEM images. AFM analysis indicates a mean surface roughness of ca. 1-2 nm for the entire thickness range both for the annealed and not-annealed copolymer films (Fig. S5), as measured over ca. 2 µm² scan area. For the composites, AFM reveals a statistically homogeneous distribution of the particles. Contrary to the pure copolymer films, a mean roughness of ca. 10-20 nm (measured over ca. 2 µm²) was observed in the composite films due to the inclusion of the particles (Fig. S6).

Crystallinity of the films

The crystalline composition of the samples has been assessed by means of a combination of XRD (Fig. 2 and Fig. S7), Raman spectroscopy (Fig. 3) and DSC (Fig. 4) techniques. The room temperature XRD patterns of the nanometric copolymer films consist of a well-defined, intense peak at 2θ = 19.75°, which has been described in the literature as the sum of the diffractions in planes (110) and (200), characteristic of the polar phase of P(VDF-TrFE) [32]. On the other hand, the 2.5 and 30 µm thick films of the pure P(VDF-TrFE) display some broader signals on the low-angle side of the main peak, which might be an indication for the formation of other polymorph(s), amorphous parts or defective phases [17,33-34].

The XRD patterns of the composites consist of the superposition of diffraction peaks of the SCO particles (around ca. 2θ = 10.5° and 2θ = 18°) and that of the polar phase of P(VDF-TrFE) (around 2θ = 19.75°). When compared to the diffraction patterns of the neat powders [26], we remark the absence of diffraction peaks in the angular domain between 22-28° where intense Bragg peaks appear in the diffractograms of randomly oriented particles. We thus conclude that some preferential orientation must take place within the composite film. This kind of anisotropy is not surprising for strongly anisometric particles and may have important consequences on the (electro)mechanical

properties of the composites. We note also that when normalizing the diffractograms of composite films of different thickness to the 2θ = 19.75° peak, the 2θ = 10.5° peaks closely overlap. This finding proves that the polar phase content is almost independent of the film thickness. From the diffraction patterns, we have estimated the apparent mean size of the crystalline domains (τ) of the low-temperature, polar phase in the different samples for different film thicknesses using the Scherrer formula [35]:

$$\tau = \frac{k\lambda}{\gamma \cos\theta} \quad (1)$$

where k is a dimensionless shape factor, λ the X-ray wavelength, γ the line broadening at half the maximum intensity and θ the diffracted Bragg angle. The calculated values are shown in Figure 2c for different film thicknesses. Some caution must be taken concerning the absolute values of τ, because different factors may contribute to the peak broadening besides the crystallite size [35]. Nevertheless, the comparison of different samples and different film thicknesses is meaningful and demonstrates that neither the film thickness, neither the presence of the filler has a substantial impact on the apparent mean size (*ca.* 10 ± 1 nm) of the crystalline domains of the polar phase in the matrix.

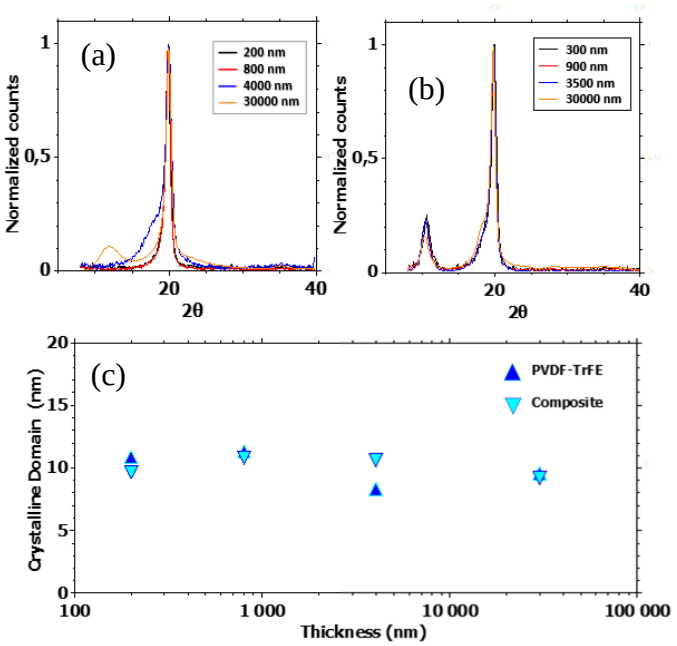

Figure 2. GI-XRD patterns of spray-coated (a) P(VDF-TrFE) and (b) composite films of different thicknesses. (c) Apparent crystalline domain size of the low-temperature phase in the pure P(VDF-TrFE) and composite samples as a function of the film thickness. (N.B. The 30 µm films were measured in Bragg-Brentano geometry.)

Representative Raman spectra acquired for pure copolymer and composite films at 20 °C and 110 °C are depicted in Figure 3. For both samples, one can clearly observe the characteristic symmetric CF_2 stretching modes of the crystalline polar and non-polar phases around 840 and 800 cm^{-1}, respectively [36]. The (reversible) decrease of the former at the expense of the latter at 110 °C denotes the Curie transition from the polar, low-temperature phase to the paraelectric phase, both in the pure copolymer and in the composite films. At room temperature, both the pure polymer and composite films mainly present the expected polar phase.

DSC analysis was performed on the different samples starting from ambient temperature up to the fusion temperature of the polymer. The corresponding thermograms are displayed in Figure 4 and the data extracted from the thermograms are summarized in Tables 1-2. For the pure copolymer, one can depict two endothermic peaks in the heating curve that can be assigned to the Curie transition from the ferroelectric phase to the paraelectric phase (T_C ~110 °C) and to the melting of the crystalline paraelectric phase (T_m ~150 °C), respectively [37]. The well-defined melting peaks appear in each sample around the same temperature. Interestingly, the Curie transition is characterized actually by two overlapping peaks, which indicates the co-existence of two ferroelectric phases in the material – including possibly a defective ferroelectric phase [34]. A simple visual examination of the thermograms reveals that the Curie peaks in the 300 nm thick film downshift in temperature, decrease in area and change proportions. This behaviour indicates changes in the crystallinity of the film (e.g. formation of defects, microstructural changes, etc.).

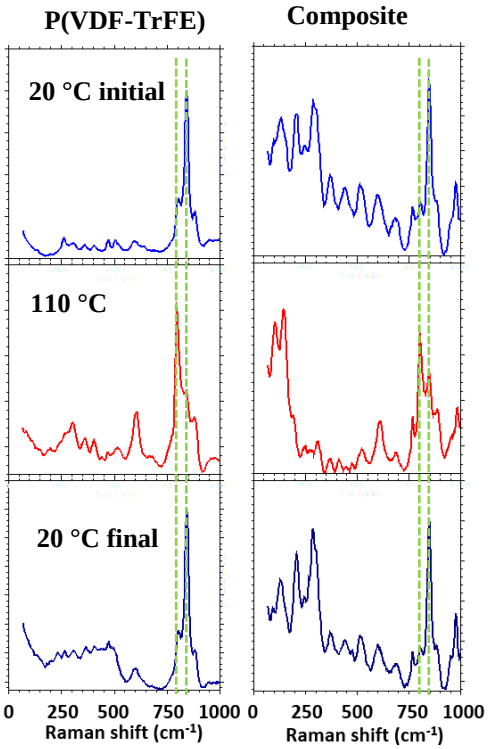

Figure 3. Raman spectra acquired at 20 °C (before heating), 110 °C and 20 °C (after heating) for pure P(VDF-TrFE) (left panel) and composite (right panel) films of 800 nm thickness. The dashed lines show the markers of the para- and ferroelectric phases at 800 and 840 cm^{-1}, respectively.

The DSC thermograms of the composites display an additional peak due to the spin transition in the filler near T_{SCO} = 77 °C. A first remark we can make is that the melting temperatures are not considerably altered by the presence of the filler, whereas the Curie temperatures are slightly reduced. Similar to the pure

copolymer, one can note a significant modification of the Curie peak in the thinnest film (400 nm). Interestingly, in this sample the phase transition of the filler is shifted to higher temperatures, overlapping thus the Curie peak. This finding is obviously crucial as for the prospects of developing synergies between the electroactive matrix and the SCO-active filler [24-25]. In a more quantitative manner, crystallinity of P(VDF-TrFE) can be related to the enthalpies associated with the melting (ΔH_m) and the Curie transition (ΔH_C). Crystallinity (χ_c) is then calculated using the following equation [37]:

$$\chi_C = \frac{\Delta H_C + \Delta H_m}{\Delta H_\infty} \times 100 \qquad (2)$$

where ΔH_∞ is the theoretical melting enthalpy value for the 100 % crystalline copolymer. By comparison with the pure PVDF and PTrFE, ΔH_∞ has been estimated as 91.5 J/g for a 100% crystalline P(VDF-TrFE) copolymer with 70/30 monomer ratio [37].

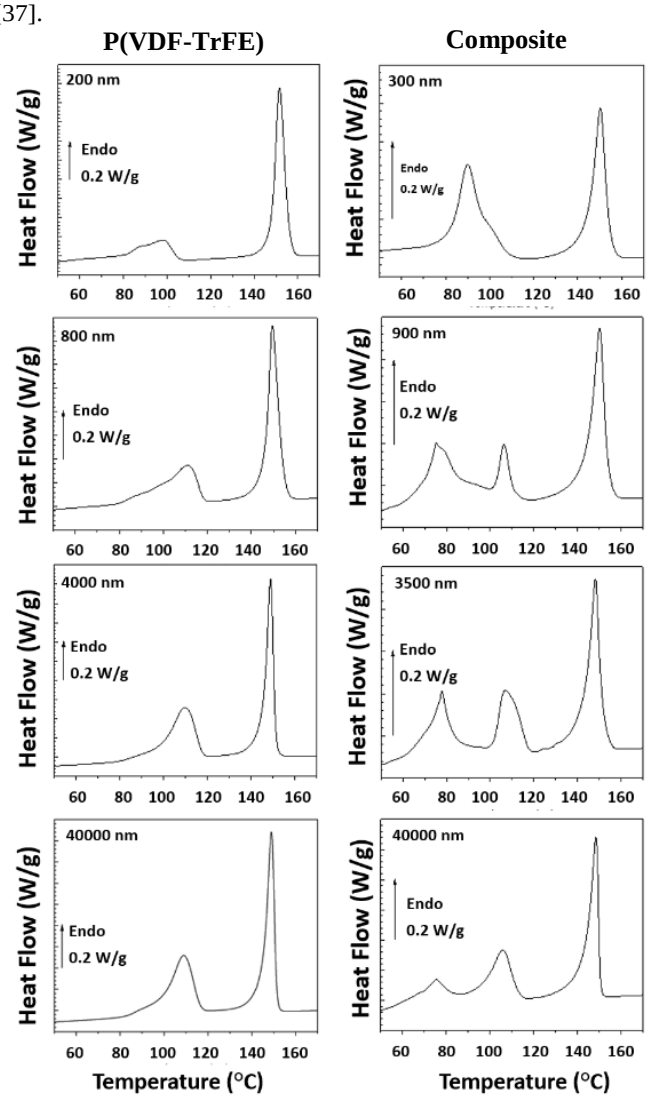

Figure 4. DSC thermograms of the pure P(VDF-TrFE) (left panel) and a composite (right panel) films for different thicknesses.

As shown by Figure 5, the apparent crystallinity of the pure copolymer films falls around 50 %, albeit with a slight reduction (43%) for the thinnest (200 nm) film. The crystallinity of the copolymer in the composite films appears similar and shows no clear trend with the film thickness. One must note, however, that for the thinnest film the peak deconvolution introduces rather high uncertainty – possibly higher than the fitting error.

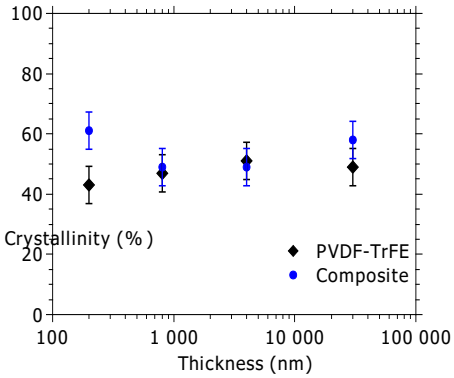

Figure 5. Crystallinity of P(VDF-TrFE) as a function of the film thickness for the pure copolymer as well as for the composite films.

Table 1. Thermal properties of the P(VDF-TrFE) films

Thickness (nm)	T_C (°C)	T_m (°C)	ΔH_C (J/g)	ΔH_m (J/g)	χ_c (%)
200	98	152	10	32	43
800	111	150	18	28	47
4000	110	149	23	26	51
30000	109	149	22	26	49

Table 2. Thermal properties of the nanocomposite films

Thickness (nm)	T_{SCO} (°C)	T_C (°C)	T_m (°C)	ΔH_C (J/g)	ΔH_m (J/g)	χ_c (%)
300	88*	101*	150	21*	19	61*
900	76	106	150	12	20	49
3500	77	107	150	13	18	49
30000	76	106	149	10	27	58

* Estimated from peak deconvolution.

Piezoelectric properties of the films

Overall, the results above confirm for each sample a reasonable crystallinity, associated mostly with the presence of the polar phase, providing thus promise for electromechanical applications. As we are handling two decades difference of thickness among the samples, the piezoelectric properties need to be assessed by different methods. Poling the thicker films was undertaken between flat metallic electrodes and the piezoelectric coefficient d_{33} was assessed using the Berlincourt method [38] (direct piezoelectricity) (see Table 3). For the pure copolymer, the obtained d_{33} value is comparable with previous reports on thick P(VDF-TrFE) films made of the same starting material [25]. The composite displays a reduced piezoelectric coefficient as it can be expected in the presence of a non-piezoelectric filler of 33 vol%. Nevertheless, this d_{33} value remains surprisingly high when compared to previous work on blade casted composite films [25]. The major difference between the two works is the significantly higher poling field, which could be reached in the

present case, arguably thanks to the best homogeneity of the spray-coated composites.

Table 3. Poling field and piezoelectric coefficient of the 30 µm thick films.

Sample	Poling field (MV/m)	d_{33} (pC/N)
P(VDF-TrFE)	70	-18.7 ± 0.05
Composite	67	-11.3 ± 0.05

The piezoelectric properties of the sub-micrometric films, spray-coated on gold substrates, were investigated by DART-PFM (converse piezoelectricity). Both poling and piezoloop measurements were conducted via the AFM tip acting as nanometric movable top electrode, giving access to local electrical behaviours. In addition, since the electromechanical activity d_{33}^{eff}, determined locally by PFM, is strongly dependent on the probed area at the surface of the sample, each local analysis was repeated on (at least) 15 different zones over the free surface of each film in order to ensure the statistical relevance of the results. Representative phase and amplitude PFM loops are shown in Figure 6 (see Fig. S8 for other samples). Well-defined, saturated and rectangular hysteresis loops are observed from the phase signal with an almost 180° phase difference, evidencing the local ferroelectricity in both the pure copolymer and the composite film.

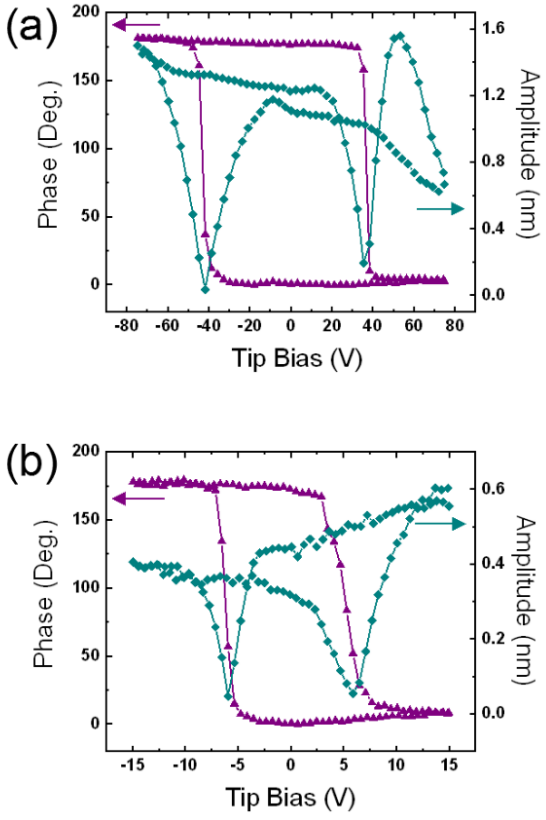

Figure 6. Local phase and amplitude PFM loops recorded on a 275 nm thick P(VDF-TrFE) film (a) and on a 400 nm thick composite film (b).

Piezoelectricity is also indicated by the characteristic "butterfly shape" of the simultaneously recorded amplitude signal [39]. The local piezoelectric coefficients d_{33}^{eff} obtained from the amplitude response [40] are given in Table 4, together with the coercive voltage/field values. As previously mentioned, the detected PFM signal is amplified by the use of the contact resonance through the DART-PFM method. This requires taking into account the quality factor *Q*, in the following relation [40]:

$$A = d_{33}^{eff} \times V_{AC} \times Q \qquad (3)$$

Thus, we have determined the d_{33}^{eff} values from the measured PFM amplitude *A* read on the piezoloops, while considering 2 V and ca. 50 for V_{AC} and *Q*, respectively. It is important to stress that the local piezoelectric coefficients extracted from PFM experiments cannot be considered as fully quantitative values, mainly due to the very strong inhomogeneity of the electric field beneath the AFM tip, the complicated calibration procedure and the poor surface/tip contact [41-42]. Nevertheless, comparison of the estimated values, ca. 9-11 pm/V for the pure copolymer and ca. 4-6 pm/V for the composite films, can be done with confidence since all piezoloops were recorded the same day under similar experimental conditions. Similar to the thick films, a higher piezoelectric coefficient was found for the pure polymer when compared to the nanocomposite films. On the other hand, the composite films displayed a much smaller coercive voltage, which can be a decisive advantage for device operation [3]. This important observation has been confirmed for another series of composite samples (not shown here), in which the coercive voltage could be maintained below 10 V for film thicknesses up to 1.5 microns. The polarization switching process in ferroelectrics is affected by many factors. Notably, the presence of the inclusions inside the matrix may provoke an enhanced nucleation of ferroelectric domains in the crystal phase at the particle/polymer interface, which promotes the ferroelectric switching. Similar effect has been observed in previous works with inorganic particles inside P(VDF-TrFE) [43].

Table 4. Coercive voltage/field and local piezoelectric coefficient of the films analyzed by PFM.

Sample	Thickness (nm)	Coercive voltage (V)	Coercive field (kV/mm)	Local d_{33}^{eff} (pm/V)
P(VDF - TrFE)	200	15 ± 3	73	-9.0
	275	36 ± 2	140	-11 ± 2
	400	38 ± 11	90	-9.6
	800	>200	N/A	N/A
Composite	300	5.8 ± 0.6	14.5	-3.6 ± 0.9
	900	12 ± 1	10	-6.3 ± 1.2

The ferroelectric switching behaviour of the films was also investigated by means of PFM lithography. Artificial domains were locally induced by applying positive and negative DC bias (exceeding the coercive voltage) to the AFM tip over rectangular areas at the free surface of the films. Out-of-plane PFM signals acquired on these areas are shown by Figure 7. Domains with "upward" (away from the substrate) and "downward" (toward the substrate) polarization, i.e. positively and negatively

polarized regions respectively, are clearly distinguished in the phase PFM images with strong contrasts. The influence of the non-polar, paraelectric phase on the switching behaviour, which was previously identified from the Raman spectra on both samples, can be ruled out since homogeneous contrasts are observed on the phase signal associated to the pure polymer (Figure 7b). This confirms the very low fraction of this non-polar phase. However, less sharply defined domains are observed in the case of composite films. This is mainly due to the concomitant effect of the higher surface roughness and the presence of non-piezoelectric fillers. Indeed, even if we do not observe fillers on the AFM topographies simultaneously recorded (Figure 7d), they are clearly visible on the surface of the films when characterized by a more suitable imaging mode, i.e. tapping mode AFM, where reduced damage or wear of the AFM tip and surface during scanning occur, as seen on Figure S6. In addition, this agrees with the nanometric lateral dimensions of the non-reversed areas observed on the PFM phase pattern (Figure 7e). However, it is worth noting that switched domains are still clearly distinguishable, denoting the good stability of the ferroelectric polarization at room temperature.

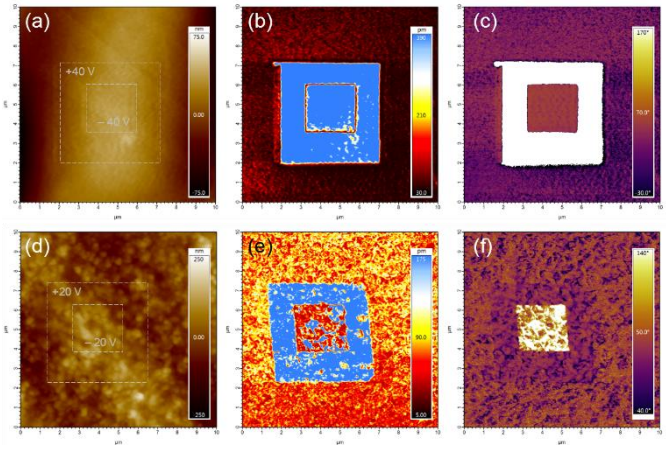

Figure 7. AFM topography (a, d), out-of-plane PFM amplitude (b, e) and phase (c, f) signals recorded just after a poling experiment at ±40 V and ±20 V for a 200 nm thick pure copolymer (a-c) and for a 300 nm thick composite film (d-f), respectively. The difference in applied polarizing voltages is due to the different V_c values determined by spectroscopic PFM for the pure and composite films. (N.B. The inverted contrasts seen on the phase PFM patterns between the two samples are due to the jump in drive frequency on the other side of the resonance during scanning.)

Conclusions

In this paper we have discussed the fabrication and properties characterization of piezoelectric P(VDF70-TrFE30) films obtained by a spray-coating method. The films manufactured by this technologically relevant casting approach are dense, homogeneous and smooth over a thickness range of more than two decades (ca. 200 nm – 30 μm). Using X-ray diffraction and Raman spectroscopy, we have shown that the main crystalline phase of the matrix is the polar phase. DSC measurements revealed a crystallinity of the pure polymer and composite samples of ca. 50 %, which is slightly altered only for the thinnest films. The films display attractive electromechanical properties, characterized by high piezoelectric coefficients. Interestingly, the composite films exhibit a marked reduction of the coercive field, which is of crucial importance for low voltage applications [3,43]. These results open up attractive perspectives for the development of P(VDF-TrFE) based electromechanical transducers. Notably, work is currently continued in our laboratories to investigate the coupling of the thermal strain arising from the SCO filler with the electromechanical properties of the copolymer matrix, which represents a promising scope for thermal energy harvesting applications.

Supporting Information

Additional sample characterization details (TEM, SEM, AFM, XRD and PFM).

Author Contributions

JEAC and TL: spray coating and film characterization, MPB and LS: particle synthesis and characterization, BM and ED: DSC and piezometry, KDF, ADC, AF and RD: PFM analysis, GM, BM and JEAC: first draft, LN and AB: supervision and funding acquisition. All authors red the draft and discussed the results.

Conflicts of interest

There are no conflicts to declare.

Acknowledgements

This work was supported by the CONACyT - Mexico (PhD grant 471690 of JEAC) and the Occitanie Region/Federal University of Toulouse (PhD grant of MPB), the ANR project NAGAM (ANR-19-CE09-0008), and by the LAAS-CNRS technology platform, a member of Renatech network. Chevreul Institute (FR 2638), Ministère de l'Enseignement Supérieur, de la Recherche et de l'Innovation, Hauts-de-France Region, Fonds Européen de Développement Régional (FEDER) and Major Domain of Interest (DIM) "Eco-Energy Efficiency" of Artois University are acknowledged for supporting and funding partially this work. Région Hauts-de-France and FEDER are acknowledged for funding the MFP-3D microscope under Program "Chemistry and Materials for a Sustainable Growth". We thank the technical assistance of Dr. Yuteng Zhang and Onkar Kulkarni. We acknowledge the referees for their careful reading and useful comments on the manuscript.

Notes and references

1 W. Xia and Z. Zhang, *IET Nanodielectr.*, 2018, **1**, 17-31.
2 T. Soulestin, V. Ladmiral, F. D. Dos Santos and B. Ameduri, *Prog. Polym. Sci.*, 2017, **72**, 16-60.
3 X. Chen, X. H and Q. D. Shen, *Adv. Electron. Mater.*, 2017, **72**, 1600460.
4 P. Martins, A. C. Lopes and S. Lanceros-Mendez, *Prog. Polym. Sci.*, 2014, **39**, 683-706.
5 C. Ribeiro *et al.*, *Nat. Protoc.*, 2018, **13**, 681-704.

6 Z. Yin, B. Tian, Q. Zhu, and C. Duan, *Polymers*, 2019, **11**, 2033.
7 J. Hafner *et al.*, *Mater. Res. Lett.*, 2021, **9**, 195-203
8 A. Toprak and O. Tigli, *J. Microelectromech. Syst.*, 2015, **24**, 1989-1997.
9 A. J. Lovinger, *Science*, 1983, **220**, 1115–1121.
10 I. Katsouras *et al.*, *Nat. Mater.*, 2016, **15**, 78-84.
11 J. Hafner *et al.*, *Nat. Commun.*, 2021, **12**, 152.
12 M. Li *et al.*, *Nat. Mater.*, 2013, **12**, 433-438.
13 E. Bellet-Amalric and J. F. Legrand, Eur. Phys. J. B, 1998, **3**, 225-236.
14 T. Furukawa, *Phase Transitions*, 1989, **18**, 143.
15 N. P. Pham, J. N. Burghartz and P. M. Sarro, *J. Micromech. Microeng.*, 2005, **15**, 691.
16 L. Yu, Y. Y. Lee, F. E. Tay and C. Iliescu, *J. Phys. Conf. Ser.*, 2006, **34**, 937.
17 Y. Li *et al.*, *Mater. Design*, 2021, **199**, 109415.
18 Z. Shen *et al.*, *IEEE Sens. J.*, 2017, **17**, 3354.
19 S. Guo *et al.*, *NDT&E Int.*, 2019, **107**, 102131.
20 K. Wang, T. Godfroid, D. Robert and A. Preumont, *Actuators*, 2021, **10**, 7.
21 J. E. Angulo-Cervera *et al.*, *Mater. Adv.*, 2021, **2**, 5057-5061.
22 S. Wang and Y. Liang, *Mater. Lett.*, 2019, **247**, 71.
23 S. Taleb, M. A. Badillo-Avila and M. Acuautla, *Mater. Design*, 2021, **212**, 110273.
24 S. Rat *et al.*, *Adv. Mater*. 2018, **30**, 1705275.
25 M. Piedrahita-Bello *et al.*, *J. Mater. Chem. C*, 2020, **8**, 6042-6051.
26 I. Suleimanov *et al.*, *French-Ukrainian J. Chem.*, 2015, **3**, 66-72.
27 B. J. Rodriguez, C. Callahan, S. V. Kalinin and R. Proksch, *Nanotechnology*, 2007, **18**, 475504.
28 P. Gütlich, A. Hauser and H. Spiering, *Angew. Chem. Int. Ed.*, 1994, **33**, 2024-2054.
29 M. D. Manrique-Juarez *et al.*, *Angew. Chem. Int. Ed.*, 2017, **129**, 8186-8190.
30 J. E. Angulo-Cervera *et al.*, *Magnetochem.*, 2021, **7**, 114.
31 M. Piedrahita-Bello *et al.*, *Mater. Horizons*, 2021, **8**, 3055.
32 R. Gregorio Jr., *J. Appl. Polym. Sci.*, 2006, **100**, 3272-3279.
33 A. Pramanick *et al.*, *Phys. Rev. B*, 2017, **96**, 174103.
34 F. Bargain, P. Panine, F. D. Dos Santos and S. Tencé-Girault, *Polymer*, 2016, **105**, 144-156.
35 J. I. Langford and A. J. C. Wilson, *J. Appl. Crystallogr.*, 1978, **11**, 102-113.
36 K. Tashiro and M. Kobayashi, *Polymer*, 1988, **29**, 426-436.
37 A. Roggero, E. Dantras and C. Lacabanne, *J. Polym. Sci. B Polym. Phys.*, 2017, **55**, 1414-1422
38 J. Hafner, M. Teuschel, M. Schneider and U. Schmid, *Polymer*, 2019, **170**, 1-6.
39 N. Balke *et al.*, *ACS Nano*, 2015, **9**, 6484-6492.
40 S. Barrau *et al.*, *ACS Appl. Mater. Interfaces*, 2018, **10**, 13092-13099.
41 T. Carlier *et al.*, *Chem. Mater.*, 2020, **32**, 7188-7200.
42 L. Collins, Y. Liu, O. S. Ovchinnikova and R. Proksch, *ACS Nano*, 2019, **13**, 8055-8066.
43 Q. D. Ling *et al.*, *Prog. Polym. Sci.*, 2008, **33**, 917-978.